

The Green's function of the mild-slope equation: The case of a monotonic bed profile

Konstadinos A. Belibassakis*

*Ship and Marine Hydrodynamics Laboratory, Department of Naval Architecture and Marine Engineering,
National Technical University of Athens, PO Box 64033, Zografos 15710, Athens, Greece*

Received 9 July 1999; received in revised form 20 March 2000

Abstract

In the present work the Green's function of the mild-slope and the modified mild-slope equations is studied. An effective numerical Fourier inversion scheme has been developed and applied to the construction and study of the source-generated water-wave potential over an uneven bottom profile with different depths at infinity. In this sense, the present work is a prerequisite to the study of the diffraction of water waves by localized bed irregularities superimposed over an uneven bottom. In the case of a monotonic bed profile, the main characteristics of the far-field are: (i) the formation of a shadow zone with an ever expanding width, which is located along the bottom irregularity, and (ii) in each of the two sectors not including the bottom irregularity the asymptotic behavior of the wave field approaches the form of an outgoing cylindrical wave, propagating with an amplitude of order $O(R^{-1/2})$, where R is the distance from the source, and wavelength corresponding to the sector-depth at infinity. Moreover, the weak wave system propagating in the shadow zone is of order $O(R^{-3/2})$, and along the bottom irregularity consists of the superposition of two outgoing waves with wavelengths corresponding to the two depths at infinity. © 2000 Elsevier Science B.V. All rights reserved.

1. Introduction

Problems of harmonic-wave interaction with two-dimensional (2D) localized scatterers or inclusions embedded in an infinite non-uniform medium, characterized by a variable index of refraction along one direction, are frequently encountered in applications related to acoustic, elastic and electromagnetic wave propagation. This class of problems is complicated by the fact that the physical properties of the medium (the index of refraction or the propagation speed) are different at infinity as approached from different directions. In this case the far-field wave pattern is not known a priori, and a standard radiation condition (e.g., the Sommerfeld condition) cannot be applied. Felsen and Marcuvitz [1] and Brekhovskikh and Godin [2] present an excellent account of solutions of acoustic and electromagnetic radiation and scattering problems in continuously stratified and layered media.

Similar problems arise in water waves, in the case where a harmonic-wave of angular frequency ω , propagating in a region of parallel bottom contours, interacts with a localized 2D bed irregularity. In this case, if the bed is mildly sloping in the region under consideration, one-equation models, such as the classical mild-slope equation [3], or the modified mild-slope equation [4–6], can be used for the description of wave propagation and diffraction. The

* Fax: +30-1-7721032.
E-mail address: kbel@fluid.mech.ntua.gr (K.A. Belibassakis)

mild-slope equation, written with respect to the velocity potential on the free surface $F=F(x, y)$, where (x, y) are the horizontal coordinates, reads as follows:

$$\nabla^2 F + \frac{\nabla(cc_g)}{(cc_g)} \nabla F + K^2(1 + \psi)F = 0. \tag{1.1}$$

In Eq. (1.1) c and c_g are the local phase and group velocities of water waves, respectively, K is the local wavenumber obtained as the positive root of the dispersion relation $\omega^2=Kg \tanh(Kh)$, and $h=h(x, y)$ is the local depth. The function $\psi=\psi(x, y)$ appearing in Eq. (1.1) is given by

$$\psi = \begin{cases} 0, & \text{for the classical mild-slope equation,} \\ \psi(k_0h; \nabla h, \nabla^2 h), & \text{for the modified mild-slope equation.} \end{cases} \tag{1.2}$$

See, e.g., [6]. The above models are widely used to predict wave properties in coastal regions, since they have been proved capable to treat general complex wave fields with satisfactory accuracy, for bottom slopes up to 1:3, or even higher [7]. Moreover, it can be easily shown that, by the substitution $\Phi = \sqrt{cc_g}F$, Eq. (1.1) reduces to the 2D Helmholtz equation [3],

$$\nabla^2 \Phi + k_{2D}^2 \Phi = 0, \quad \text{where } k_{2D}^2(x, y) = K^2(1 + \psi) - \frac{\nabla^2 \sqrt{cc_g}}{\sqrt{cc_g}}. \tag{1.3}$$

Consider now the environment presented in Fig. 1. Let $h_{2D}(x, y)$ be the 2D depth function, decomposed as follows:

$$h_{2D}(x, y) = h(x) + h_{loc}(x, y), \tag{1.4}$$

where $h_{loc}(x, y)$ denotes the 2D depth disturbance due to a localized bed irregularity, superimposed over the 1D bottom shoaling $h(x)$. We denote by $k_{2D}(x, y)$ and $k(x)$ the wavenumbers associated with the depth functions $h_{2D}(x, y)$ and $h(x)$, respectively. Let B_R be the region enclosed by a circle of radius R containing strictly inside the localized inhomogeneity, and \mathbf{n} the outward unit normal on the circle ∂B_R ; see Fig. 1. From the previous definitions, it is obvious that

$$k_{2D}(x, y) = k(x), \quad (x, y) \in \mathbb{R}^2 \setminus B_R. \tag{1.5}$$

Let $\Phi_i(x, y)$ be the (transformed) velocity potential on the free surface of a propagating wave over the 1D bottom shoaling $h(x)$, in the absence of the local irregularity $h_{loc}(x, y)$. This potential can be calculated by solving a 1D (in the x -direction) mild-slope equation; see, e.g., [4,5], or its extended versions [8,9]. In the case of an oblique-incident

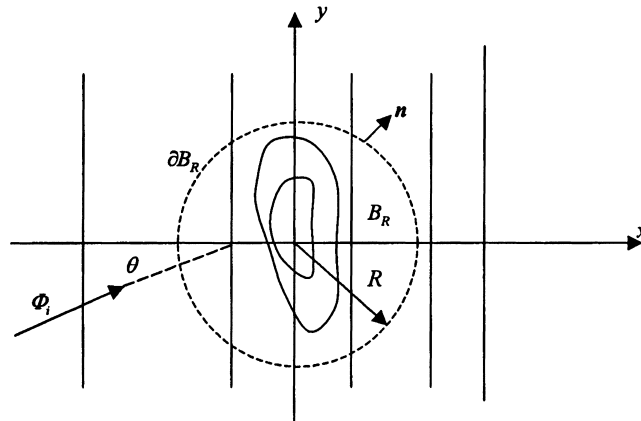


Fig. 1. Bathymetric contours of the examined environment.

wave ($\theta \neq 0$), the transverse (y) dependence can be explicitly factored out [4]. Thus, the wave potential $\Phi_i = \Phi_i(x, y)$ can be considered known (for any wave direction θ), and it will serve the purpose of the incident wave field. The presence of the localized 2D bed irregularity $h_{loc}(x, y)$ gives rise to a diffraction potential $\Phi_d = \Phi_d(x, y)$, satisfying the following equation:

$$\nabla^2 \Phi_d + k_{2D}^2(x, y) \Phi_d = \begin{cases} -(k_{2D}^2(x, y) - k^2(x)) \Phi_i, & (x, y) \in B_R, \\ 0, & (x, y) \in \mathbb{R}^2 \setminus B_R. \end{cases} \quad (1.6)$$

In order to treat the above problem it is important to know the far-field behavior of the diffracted field $\Phi_d(x, y)$. However, since the parameter $k_{2D}(x, y)$ is azimuthally anisotropic at infinity, the only a priori assumption that can be safely imposed is of qualitative nature, i.e.

$$\Phi_d(x, y) \text{ behaves like outgoing waves as } R = \sqrt{x^2 + y^2} \rightarrow \infty. \quad (1.7)$$

The major contribution of the present work is to investigate the asymptotic behavior of Φ_d as $R \rightarrow \infty$, providing quantitative information on the structure of the far-field and eliminating the vagueness of the radiation condition (1.7).

It should be mentioned here that there have been developed numerical techniques permitting the solution of Eq. (1.6), in compatibility with the qualitative radiation condition (1.7). Some of the most common techniques of this kind are the artificial or non-reflecting boundary conditions (ABCs or NRBCs), the absorbing layers and the infinite elements. All the above are introduced in conjunction with an artificial exterior boundary in order to eliminate the infinite domain and to absorb without reflection the wave energy that reaches the artificial boundary; see, e.g., the surveys by Givoli [10,11], and Tsynkov [12], and the references cited therein. However, one of the major tasks in using these techniques is the investigation of the optimum values of the involved numerical parameters (such as the position of the artificial boundaries, the coefficients of the NRBCs, the properties of the absorbing layers, or the representation of the wave field at infinity by means of the infinite-element shape functions) in order to minimize the contamination of the numerical solution by pseudo-reflections. This task is usually the most cumbersome and costly part of applications anticipated by the above methods.

A more efficient approach to treat the diffraction problem, Eqs. (1.6) and (1.7), is offered by utilizing the Green's integral formula for the representation of the diffracted field Φ_d outside the localized inhomogeneity. By assuming zero contribution from the boundary at infinity (a working hypothesis to be justified a posteriori), the Green's representation reads

$$\Phi_d(x, y) = \frac{1}{2\pi} \int_{\partial B_R} \left(\Phi_d \frac{\partial G}{\partial n} - \frac{\partial \Phi_d}{\partial n} G \right) dl, \quad (x, y) \in \mathbb{R}^2 \setminus (B_R \cup \partial B_R), \quad (1.8)$$

where the involved Green's function $G = G(x, y; x_0, y_0)$ satisfies

$$\nabla^2 G + k^2(x) G = -2\pi \delta(x - x_0, y - y_0), \quad (1.9)$$

and behaves like outgoing waves at infinity. The integral representation (1.8) shows that the determination of the far-field behavior of the solution Φ_d reduces to the far-field behavior of the Green's function G . The latter is a much more tractable problem, since the wavenumber $k(x)$ involved in Eq. (1.9) is 1D and, thus, this equation can be reduced to a 1D-model equation by applying a Fourier transform. The construction of G and the study of its far-field asymptotics is the main contribution of the present work. Moreover, the above Green's function can be exploited for the equivalent reformulation and solution of the diffraction problem as a *matching-boundary value problem* in the bounded subdomain enclosing the bottom irregularity. See, e.g., [13] for the diffraction of water waves by a localized bed irregularity in a constant depth region, and [14] for the acoustic scattering by a compact obstacle in a stratified host medium. For all the above purposes, an accurate and efficient calculation of the Green's function (1.9) is necessary. Unfortunately, explicit analytical expressions of Green's functions for the Helmholtz equation in

anisotropic media are available only for a restricted class of wavenumber profiles. For a review see, e.g., [1,15–17]. Thus, it is necessary to resort to numerical calculations.

In the present work an effective numerical Fourier inversion scheme will be applied to the construction and study of the source potential, Eq. (1.9), in a continuously layered medium with different properties at infinity. The contents of the present work are organized as follows: in Section 2, the differential formulation of the problem is presented, in the physical and in the Fourier-transformed domain. It is assumed that the depth function and, thus, the index of refraction are continuously varying only in a finite interval, where also the source is located, and attain constant, but different, values in the adjacent semi-infinite intervals. By applying domain decomposition, the transformed problem is reformulated as a transmission problem in the finite interval containing the parameter irregularity, in a form suitable for numerical calculations. Care is taken for extending the formulation in the complex Fourier domain, permitting, at a subsequent step, a robust numerical inversion by means of FFT with a simultaneous elimination of the aliasing effect. Similar treatment has been previously reported for applications involving the Hankel transform for 3D acoustic wave propagation in plane-stratified media [18], in homogeneous media above an impedance plane [19], and in waveguides [20,21].

In Section 3, an analytical solution in the physical domain is derived in the characteristic case of a simply-discontinuous infinite medium [1,2], with the source located at the interface. This solution, except of its own significance, can serve as a benchmark for the assessment of numerical models developed for treating more general environments of the same kind. In this connection, it is also exploited in the present work for checking the accuracy of the numerical Fourier inversion, which is presented in Section 4. The principal far-field asymptotics of the source field in the case of a simply-discontinuous infinite medium are studied in Section 3, and are further exploited in Section 5, where the far-field of the source potential in a region characterized by a smooth 1D bottom variation with different depths at infinity is examined.

The present analysis demonstrates that, in the case of a continuous, monotonic bed profile, the far-field pattern exhibits common features with the simply-discontinuous wavenumber case. The main characteristics of the far-field, up to the leading order $O(R^{-1/2})$ are: (i) the formation of a shadow zone with an ever expanding width, which is located along the bottom irregularity, and (ii) in each of the two sectors not including the bottom irregularity the asymptotic behavior of the wave field approaches the form of an outgoing cylindrical wave propagating with wavelength corresponding to the sector-depth at infinity. Moreover, the weak wave system propagating along the bottom irregularity is of order $O(R^{-3/2})$, and consists of the superposition of two outgoing waves with wavelengths corresponding to the two depths at infinity. Finally, a transverse resonance condition is derived, in the form of an eigenvalue integral equation, which could be found useful in recognizing the emergence of poles in the case of non-monotonic profiles leading to duct propagation [1,3]. This could happen, e.g., in the case of diffraction of an oblique-incident wave by a localized scatterer superimposed over a smooth underwater ridge, where the appearance of guided modes (or trapped waves) along the bottom irregularity, at specific frequencies, is possible ([3], Chapter 4.6).

2. Differential formulation of the problem

Consider the continuously layered environment which is schematically presented in Fig. 2. The wave field is excited by a monochromatic point source of angular frequency ω . It is assumed that the index of refraction $n(x)=k(x)/k_*$, where $k(x)$ is given by Eq. (1.3) and $k_*= \max\{k(x), x \in \mathbb{R}\}$ is the reference wavenumber of the medium, exhibits an arbitrary 1D variation in a finite interval $[a, b]$. Thus, the distributions of $n(x)$ and $k(x)$ are characterized by parallel and straight contours lying between two regions of constant, but different, values, $k=k_1$ and $k=k_3$; see Fig. 2. Without loss of generality it is assumed that $k_3 > k_1$.

The wavenumber, $k=k(x) > 0$, is considered to be a smooth function defined over the real axis \mathbb{R} . In accordance with the previous description

$$k(x) = k(a) = k_1 \quad \text{for all } x \leq a, \quad k(x) = k(b) = k_3 \quad \text{for all } x \geq b. \quad (2.1)$$

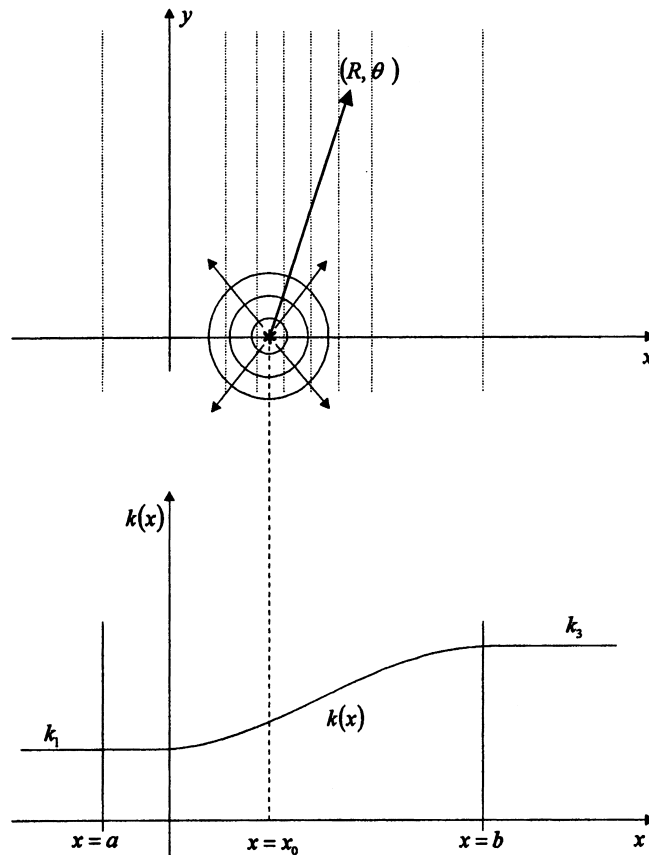


Fig. 2. Wavenumber (or index of refraction) variation. The position of the source is denoted by using an asterisk.

Thus, the domain $D = \mathbb{R}^2$ is decomposed into three subdomains $D^{(m)}$, $m=1, 2, 3$, where $D^{(1)}$ is the constant-parameter subdomain $x \leq a$, $D^{(3)}$ the constant-parameter subdomain $x \geq b$, and $D^{(2)}$ the variable parameter subdomain lying between $D^{(1)}$ and $D^{(3)}$. Let us assume the following representation of the source-generated potential:

$$\Phi(\mathbf{r}, \mathbf{r}_0; t) = \text{Re}\{\Phi(\mathbf{r}, \mathbf{r}_0; k)\exp(-i\omega t)\}, \tag{2.2}$$

where $i = \sqrt{-1}$ and $\mathbf{r}=(x, y)$ denotes the field point. According to Eq. (1.9) the problem is formulated in terms of the frequency-dependent potential $\Phi = \Phi(\mathbf{r}, \mathbf{r}_0; k)$ as follows:

$$\frac{\partial^2 \Phi}{\partial x^2} + \frac{\partial^2 \Phi}{\partial y^2} + k^2(x)\Phi = -2\pi \delta(\mathbf{r} - \mathbf{r}_0), \quad \mathbf{r} \in D, \tag{2.3a}$$

Φ along with its spatial derivatives is bounded and at any direction θ behaves like outgoing waves as

$$R = |\mathbf{r} - \mathbf{r}_0| = \sqrt{(x - x_0)^2 + (y - y_0)^2} \rightarrow \infty, \tag{2.3b}$$

where $\mathbf{r}_0=(x_0, y_0)$ is the location of the point source. All derivatives appearing in Eqs. (2.3a) and (2.3b) are with respect to the field-point variables $\mathbf{r}=(x, y)$. Without loss of generality it is assumed that $\mathbf{r}_0 \in D^{(2)}$ and $y_0=0$. The boundary value problem (2.3a) and (2.3b) will be referred to as the *original wave problem* $\mathcal{P}(D, k, \mathbf{r}_0)$. Since the geometry of the domain and the forcing of this problem are symmetric with respect to y , the solution $\Phi(\mathbf{r}, \mathbf{r}_0; k)$

exhibits the same symmetry. It is possible to reduce the dimensionality of $\mathcal{P}(D, k, \mathbf{r}_0)$ by taking the Fourier transform with respect to y . The transformed wave potential will be denoted by $\varphi(x, x_0; \xi)$. The following pair of equations clarifies our conventions regarding the 2π -factors and exponent signs in the Fourier transform:

$$\varphi(x, x_0; \xi) = \frac{1}{2\pi} \int_{-\infty}^{+\infty} \Phi(\mathbf{r}, \mathbf{r}_0; k) e^{-iy\xi} dy, \quad (2.4a)$$

$$\Phi(\mathbf{r}, \mathbf{r}_0, k) = \int_{-\infty}^{+\infty} \varphi(x, x_0; \xi) e^{+iy\xi} d\xi. \quad (2.4b)$$

2.1. The Fourier-transformed problem

Applying the Fourier transform to the problem $\mathcal{P}(D, k, \mathbf{r}_0)$, we obtain the following family of 1D wave problems:

$$\frac{\partial^2 \varphi}{\partial x^2} + (k^2(x) - \xi^2)\varphi = -\delta(x - x_0), \quad -\infty < x < \infty, \quad (2.5a)$$

φ along with its spatial derivatives is bounded and behaves like outgoing waves as

$$|x| \rightarrow \infty \quad (2.5b)$$

for all $\xi \in \mathbb{R}$. The family of problems (2.5a) and (2.5b) will be referred to as the *transformed wave problem* $\mathcal{P}_\xi(k, x_0)$. The source-point being fixed, the transformed wave potential $\varphi(x, x_0; \xi)$ will be occasionally denoted by $\varphi(x; \xi)$. Since the source potential Φ is y -symmetric, the transformed wave potential will also be symmetric with respect to the Fourier parameter ξ . Thus, it is possible to consider the problem $\mathcal{P}_\xi(k, x_0)$ only for $\xi \in \mathbb{R}^+$, and then extend the solution to $\xi \in \mathbb{R}^-$ by symmetry, i.e.

$$\varphi(x, x_0; \xi) = \varphi(x, x_0; -\xi), \quad \xi \in \mathbb{R}^-. \quad (2.6)$$

Obviously, $\varphi(x, x_0; \xi)$ is a continuous function of both arguments x, x_0 , with a simple discontinuity in its first derivative at $x=x_0$. The existence and uniqueness of the solution of $\mathcal{P}_\xi(k, x_0)$, for a layered medium, is discussed by other authors; see, e.g., [14,22]. Furthermore, it is known [1], that $\varphi(x; \xi)$ exhibits branch-points located at $\xi = \pm k_m$, $m=1, 3$ (see Eq. (2.8)), and decays exponentially for large values of the Fourier parameter,

$$\varphi(x, x_0; \xi) \approx \frac{\exp(-\xi|x - x_0|)}{2\xi}, \quad \xi \rightarrow \infty. \quad (2.7)$$

WKB asymptotic solutions to $\mathcal{P}(D, k, \mathbf{r}_0)$ and $\mathcal{P}_\xi(k, x_0)$ can be constructed by the direct ray-optical method and by the asymptotic evaluation of radiation integrals [1]. However, these solutions are valid only in the high-frequency case or in the case of a slowly varying medium ($|dk/dx| \ll k^2$). In the present work we are interested in the complete solution of the problem and the study of its asymptotic behavior in the far-field.

We shall now proceed to an equivalent reformulation of the problem $\mathcal{P}_\xi(k, x_0)$ as a *transmission problem* in the variable parameter subinterval $d^{(2)}=(a, b)$. To this aim, for any value of the Fourier parameter $\xi \in \mathbb{R}^+$, the following, general representations of the potentials $\varphi^{(m)}(x, x_0; \xi)$, $m=1, 3$, in the two semi-infinite intervals $d^{(1)}=(-\infty, a]$ and $d^{(3)}=(b, \infty]$ will be used:

$$\varphi^{(m)}(x, x_0; \xi) = C^{(m)}(x_0; \xi) \exp(i|x - x_0| \mathcal{K}^{(m)}(\xi)), \quad \text{where } \mathcal{K}^{(m)}(\xi) = \sqrt{k_m^2 - \xi^2}, \quad m = 1, 3. \quad (2.8)$$

The coefficients $C^{(m)}(x_0; \xi) \equiv C^{(m)}$, $m=1, 3$, will be determined by means of the matching conditions at the interfaces $x=a$ and $x=b$, requiring C^1 — continuity of the wave potential. Exploiting the representations (2.8) the problem $\mathcal{P}_\xi(k, x_0)$ can be reformulated as a *transmission problem* in the bounded interval $d^{(2)}$ as follows:

Problem ($\mathcal{P}_\xi^T(k, x_0)$). Find the potential $\varphi^{(2)}(x, x_0; \xi)$ defined in $d^{(2)}$ satisfying the equations:

$$\frac{\partial^2 \varphi^{(2)}}{\partial x^2} + (k^2(x) - \xi^2)\varphi^{(2)} = -\delta(x - x_0), \quad a < x < b, \tag{2.9a}$$

$$\frac{\partial \varphi^{(2)}}{\partial x} + i\sqrt{k_1^2 - \xi^2}\varphi^{(2)} = 0, \quad x = a, \tag{2.9b}$$

$$\frac{\partial \varphi^{(2)}}{\partial x} - i\sqrt{k_3^2 - \xi^2}\varphi^{(2)} = 0, \quad x = b. \tag{2.9c}$$

Having obtained the solution $\varphi^{(2)}(x, x_0; \xi)$ of $\mathcal{P}_\xi^T(k, x_0)$, the coefficients $C^{(m)}$ of the expansions (2.8) in $d^{(m)}$, $m=1, 3$, are then given by

$$C^{(1)} = \varphi^{(2)}(x = a; \xi)\exp(-i|a - x_0|\mathcal{K}^{(1)}(\xi)), \quad C^{(3)} = \varphi^{(2)}(x = b; \xi)\exp(-i|b - x_0|\mathcal{K}^{(1)}(\xi)). \tag{2.10}$$

2.2. Extension of the formulation to complex ξ

For obtaining the numerical solution of the problem $\mathcal{P}(D, k, \mathbf{r}_0)$, the Fourier inversion (2.4b) will be evaluated by an efficient application of the discrete Fourier transform (see Section 4). The latter is based on the truncation of the infinite interval of integration and on the discretization (sampling) of the integrand in the finite subinterval. However, it is well known that undersampling in the ξ -domain causes aliasing in the physical y -domain. An effective way to eliminate the aliasing problem is to move the integration contour in the complex plane. Thus, we need to consider the transformed wave problem for complex $\xi = \xi_1 + i\xi_2$ and, especially, for ξ lying in a strip $S_{cd} = \{-\infty < \xi_1 < \infty, c < \xi_2 < d\}$ parallel to the real- ξ axis (see Fig. 3). The condition of symmetry (2.6) is naturally extended in the complex domain as follows:

$$\varphi(x, x_0; \xi_1 + i\xi_2) = \varphi(x, x_0; -\xi_1 - i\xi_2), \quad \xi \in S_{cd}. \tag{2.11}$$

Under specific conventions that will be introduced below for treating the multi-valued functions $\mathcal{K}^{(m)}(\xi)$, $m=1, 3$, in the complex domain, we assume that the representations in $d^{(m)}$ remain valid for lying in the right-half strip

$$\xi \in S_{c0}^+ = \{0 < \xi_1 < \infty, c < \xi_2 \leq 0\}, \tag{2.12}$$

where $c < 0$ is a small negative number, and its symmetric left-half strip S_{0d}^- with respect to the origin; see Fig. 3.

The branch-points of the functions $\mathcal{K}^{(m)}(\xi) = \sqrt{k_m^2 - \xi^2}$, are located symmetrically on the real ξ -axis at the points, $\xi = \pm k_m$, $m=1, 3$. We define the associated cuts along the real ξ -axis, as presented in Fig. 3 by using thick

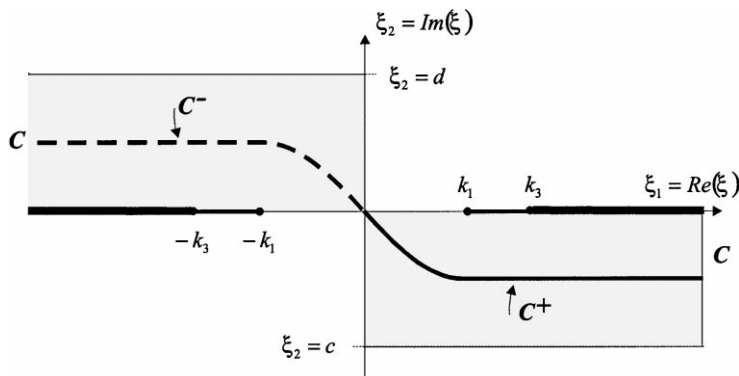


Fig. 3. Integration path for the Fourier inversion in the complex ξ -domain.

lines, so that the imaginary part of $\mathcal{K}^{(m)}(\xi)$ takes positive values below the real axis and along the branch cut emanating from $\xi = +k_m$, $m=1, 3$, and above the real axis along the branch cut emanating from $\xi = -k_m$, $m=1, 3$. Thus, for $\xi \in S_{c0}^+ \cup S_{0d}^-$, it holds $\text{Im}\{\mathcal{K}^{(m)}(\xi)\} > 0$. On the basis of the above considerations, and under the assumption that the functions $\{\mathcal{K}^{(m)}(\xi), m=1, 3\}$ remain regular in $S_{c0}^+ \cup S_{0d}^-$, and well-behaved at infinity for

$$\xi \in S_{c0}^+ \cup S_{0d}^-, \quad |\xi| \rightarrow \infty, \quad (2.13)$$

the representations (2.8) satisfy all requirements of the transformed problem $\mathcal{P}_\xi(k, x_0)$ in $d^{(m)}$, $m=1, 3$, including the radiation condition, Eq. (2.5b). Thus, the formulation is extended to complex ξ . On the basis of the theory of analytic functions, the Fourier inversion can be equivalently calculated by moving the integration contour (C) in the complex domain within $S_{c0}^+ \cup S_{0d}^-$. Furthermore, by taking the contour to be symmetric with respect to the origin, see Fig. 3, and using Eq. (2.11), the Fourier inversion formula is written as follows:

$$\Phi(\mathbf{r}, \mathbf{r}_0; \mu) = 2 \int_{\xi \in (C^+)} \varphi(x, x_0; \xi) \cos(\xi y) d\xi, \quad (2.14)$$

where (C^+) is the symmetric part of (C) lying in S_{c0}^+ . It is clear from the above discussion that for the solution of the problem to satisfy the radiation condition (2.3b), the integration path in Eq. (2.4b) must be considered indented below the positive, and above the negative, real ξ -axis [1,2]. By the above choice of the position of the branch cuts, the following relations are valid on the real ξ -axis:

$$\mathcal{K}^{(m)}(\xi) = \sqrt{k_m^2 - \xi^2} = \begin{cases} i\sqrt{\xi^2 - k_m^2}, & |\xi| > k_m, \\ \sqrt{k_m^2 - \xi^2}, & |\xi| < k_m, \end{cases} \quad m = 1, 3, \quad (2.15)$$

see also [23].

3. The case of a simply-discontinuous medium

The classical problem of the field generated by an acoustic point source located at a finite distance from an interface between two homogeneous media, and its far-field asymptotics, both in two and in three dimensions, has received great attention in the literature of acoustic and electromagnetic wave propagation. A thorough presentation including also an elucidating discussion on the details of the solution of this problem can be found in the monographs by Felsen and Marcuvitz [1] and Bleistein [24], in two and three dimensions, and in [2], in three dimensions. In all the above works the reference integral method (saddle point or steepest decent method) is applied to the determination and study of the behavior of the field at relatively large observation distances from the source, where the representation (Fourier) integrals are amenable to asymptotic evaluation.

In the present section we shall review the fundamental aspects of the solution of the 2D source problem, in the special case where the source is assumed to be located exactly on the interface of a medium characterized by a simply-discontinuous wavenumber distribution of the form:

$$k(x) = k_1 + (k_3 - k_1)U(x - x_0), \quad (3.1)$$

where $U(x-x_0) = \frac{1}{2} + \frac{1}{2} \text{sign}(x-x_0)$ is the *Heaviside* unit-step function. For later convenience we shall refer to this as the k_1 - k_3 case. For this problem, an alternative analytical solution in the physical space, in the form of a double-layer potential induced by a generalized dipole distribution over the interface, will be first derived. This result will be exploited in the next section for the assessment of the numerical Fourier inversion scheme, developed for treating the source problem in a general, continuously layered medium. Moreover, as it will be illustrated in Section 5, the far-field asymptotics of the k_1 - k_3 problem exhibit common features with the source-generated field in a general continuously layered medium, characterized by a monotonic wavenumber (or index of refraction) profile in the middle interval $d^{(2)} = [a, b]$ with the same end-values at $x=a$ and $x=b$.

In the k_1 - k_3 case $d^{(2)} = \emptyset$, and the solution of the Fourier-transformed problem $\mathcal{P}_\xi(k, x_0)$ in $d^{(m)}$, $m=1, 3$, is obtained from Eqs. (2.5a) and (2.5b) as follows:

$$\varphi^{(m)}(x, x_0; \xi) = \frac{i}{\sqrt{k_1^2 - \xi^2} + \sqrt{k_3^2 - \xi^2}} \exp(i|x - x_0|\mathcal{K}^{(m)}(\xi)), \quad m = 1, 3, \tag{3.2a}$$

where $\mathcal{K}^{(m)}(\xi)$ are given by Eq. (2.8). Obviously, in this case

$$C^{(1)}(\xi) = C^{(3)}(\xi) = \frac{i}{\sqrt{k_1^2 - \xi^2} + \sqrt{k_3^2 - \xi^2}}. \tag{3.2b}$$

The above result is also confirmed by the analysis of Felsen and Marcuvitz [1] and Bleinstein [24]. Then, by using Eq. (2.15), the inverse Fourier transform (2.4b) of the potential (3.2) at $x=x_0$, providing the field $\Phi(x=x_0, y)$ along the interface, can be derived in closed form; see ([25], Chapter 9, paragraph 130/134). Restricting ourselves only to the symmetrical part of the physical domain ($y>0$), the analytical result is

$$\mu(y) \equiv \Phi(x = x_0, y) = \frac{\pi i}{k_1^2 - k_3^2} \left(\frac{k_1 H_1^{(1)}(k_1 y)}{y} - \frac{k_3 H_1^{(1)}(k_3 y)}{y} \right), \tag{3.3}$$

where $H_1^{(1)}$ is the *Hankel* function of the first kind and first order. Eq. (3.3) is also reported in ([1], p. 625). It is important to notice here the following facts concerning the distribution $\mu(y)$ on the $x=x_0$ axis:

1. The distribution $\mu(y)$ presents a logarithmic (weak) singularity $\mu(y) \sim (-i/\pi)\ln(y)$, as $y \rightarrow 0$, and a decay $|\mu(y)| \sim y^{-3/2}$, as $y \rightarrow \infty$.
2. Eq. (3.3) reduces to the Green's function of the homogeneous Helmholtz equation $\Phi(x = x_0, y) = (i\pi/2) H_0^1(k_* y)$, as $k_1 \rightarrow k_3 = k_*$.

By substituting Eq. (3.3) to the Fourier inversion formula (2.4b) and by applying the convolution theorem for generalized functions [26,27], we obtain after some algebra the following expression for the source field in $D^{(m)}$, $m=1, 3$:

$$\Phi(x \in d^{(m)}, y) = -\frac{\pi}{2} \frac{k_m(x - x_0)\text{sign}(x - x_0)}{k_1^2 - k_3^2} \int_{t=-\infty}^{t=\infty} \left(\frac{k_1 H_1^{(1)}(k_1|t|)}{|t|} - \frac{k_3 H_1^{(1)}(k_3|t|)}{|t|} \right) \frac{H_1^{(1)}(k_m R_t)}{R_t} dt, \tag{3.4}$$

where $R_t = \sqrt{(x - x_0)^2 + (y - t)^2}$. Clearly, Eq. (3.4) is a representation of the solution as the potential induced by a double-layer distribution over the interface $x=x_0$, with intensity $\mu(y)$ given by Eq. (3.3). The latter result is compatible with Eq. (3.3) in the limit $x \rightarrow x_0$. The above formulae provide us with an analytical expression of the solution of the source field in the case of a simply-discontinuous layered medium in the whole physical domain. Numerical demonstrations of these formulae will be given in Section 4.

Apart from its own significance, the above result can serve as a benchmark for the assessment of various numerical models developed for treating more general environments of the same kind. In this connection, it will be used in the next section in order to demonstrate the effectiveness of the numerical Fourier inversion scheme developed for treating the source problem $\mathcal{P}(D, k, \mathbf{r}_0)$ in the case of an environment characterized by a general profile $k(r)$. Before proceeding to that, we shall briefly review the structure and the singularities of the transformed wave potential $\varphi(x, x_0; \xi)$ in the k_1 - k_3 case. This information will be further exploited in Section 5, where the principal far-field asymptotics of the wave field, in the general $k(x)$ case, will be derived.

3.1. The structure and the ξ -singularities of the transformed potential

It is obvious from Eqs. (3.2a) and (3.2b) that, in the k_1 - k_3 case, the transformed wave potential $\varphi(x, x_0; \xi)$ is a continuous and bounded function all over the real ξ -axis, presenting a decay

$$\varphi \sim |\xi|^{-1} \exp(-|x - x_0| \mathcal{K}^{(m)}(\xi)), \quad |\xi| \rightarrow \infty, \quad m = 1, 3, \quad (3.5)$$

in agreement with Eq. (2.7). As already mentioned, the source potential $\varphi(x, x_0; \xi)$, being a function of $\mathcal{K}^{(m)}(\xi)$, exhibits branch-points at $\xi = \pm k_1$ and $\xi = \pm k_3$. At these points, the first ξ -derivative of $\varphi(x, x_0; \xi)$ exhibits weak (absolutely integrable) singularities of the form

$$\left| \frac{\partial \varphi(x, x_0; \xi = \pm k_m)}{\partial \xi} \right| \sim |k_m - \xi|^{-1/2}, \quad m = 1, 3. \quad (3.6)$$

Using Eq. (2.15), we observe from Eqs. (3.2a) and (3.2b) that the intensity of the singularities at $\xi = \pm k_3$ weakens exponentially as we move away from the source-point in the subinterval $d^{(1)}$ ($x < x_0$), where the wavenumber and the index of refraction is assumed smaller ($k_1 < k_3$). On the other hand, these singularities persist in the whole subinterval $d^{(3)}$ ($x > x_0$), where the index of refraction is assumed greater, leading to a more complicated wave pattern on this side ($D^{(3)}$) of the physical space.

3.2. The far-field asymptotics of the solution in the k_1 - k_3 case

The far-field asymptotics of the source-generated field $\Phi(\mathbf{r}, \mathbf{r}_0; k)$ in the k_1 - k_3 case can be easily derived from the analysis of Felsen and Marcuvitz [1] and Bleistein [22], by letting the source to reach the interface. In these works the method of *steepest descent* [2,28] is applied, including the higher order $O(k_* R)^{-3/2}$ diffraction effects from the branch-cut integral contributions associated with the appearance of the lateral wave in $d^{(3)}$.

In the present subsection we are interested in reviewing the principal $O(k_* R)^{-1/2}$ far-field structure of the potential $\Phi(\mathbf{r}, \mathbf{r}_0; k)$ given by Eqs. (3.3) and (3.4). This can be easily accomplished by applying the method of *stationary phase* [2,28]. By substituting Eq. (3.2a) into the Fourier inversion formula (2.4b), and restricting ourselves to the symmetrical part $y > 0$ of the physical domain D , we obtain

$$\Phi^{(m)}(\mathbf{r}, \mathbf{r}_0; k) = \int_{\xi=-\infty}^{\infty} C^{(m)}(\xi) \exp(ik_* R S^{(m)}(R, \theta; k)) d\xi, \quad m = 1, 3, \quad (3.7)$$

where $R = \sqrt{(x - x_0)^2 + y^2}$ is the distance from the source, $\theta = \tan^{-1}(y/(x - x_0))$ is the azimuthal angle with respect to the source-point, $k_* = \max\{k\}$, and $S^{(m)}(R, \theta; k)$ is the phase function

$$S^{(m)}(R, \theta; k) = \frac{1}{k_*} [|\cos \theta| \sqrt{k_m^2 - \xi^2} + \sin \theta \xi], \quad m = 1, 3. \quad (3.8)$$

By breaking the integral (3.7) into three parts: $\xi \in (-\infty, -k_m) \cup [-k_m, k_m] \cup (k_m, \infty)$, and by using Eq. (2.15), we can see that the contributions of the first and third parts diminish exponentially as $R \rightarrow \infty$. For $\xi \in [-k_m, k_m]$ the phase (3.8) admits only real values, and thus, for this part, the stationary phase method is applicable. The points of stationarity of the phase function $S^{(m)}(R, \theta)$ are directly determined by setting its first ξ -derivative equal to zero,

$$\xi_{\text{st}}^{(m)} = k_m \sin \theta, \quad m = 1, 3. \quad (3.9)$$

By calculating the values of the second ξ -derivative of the phase function $S^{(m)}(R, \theta)$ at points of stationarity $\xi = \xi_{\text{st}}^{(m)}$, $m=1,3$, we finally obtain

$$\Phi^{(m)}(\mathbf{r}, \mathbf{r}_0; k) = \frac{i\pi}{2} \exp\left(i\left(k_m R - \frac{\pi}{4}\right)\right) \sqrt{\frac{2}{\pi k_m R}} F(\theta; k) + O\left(\frac{1}{k_* R}\right)^{3/2}, \quad m = 1, 3, \quad (3.10a)$$

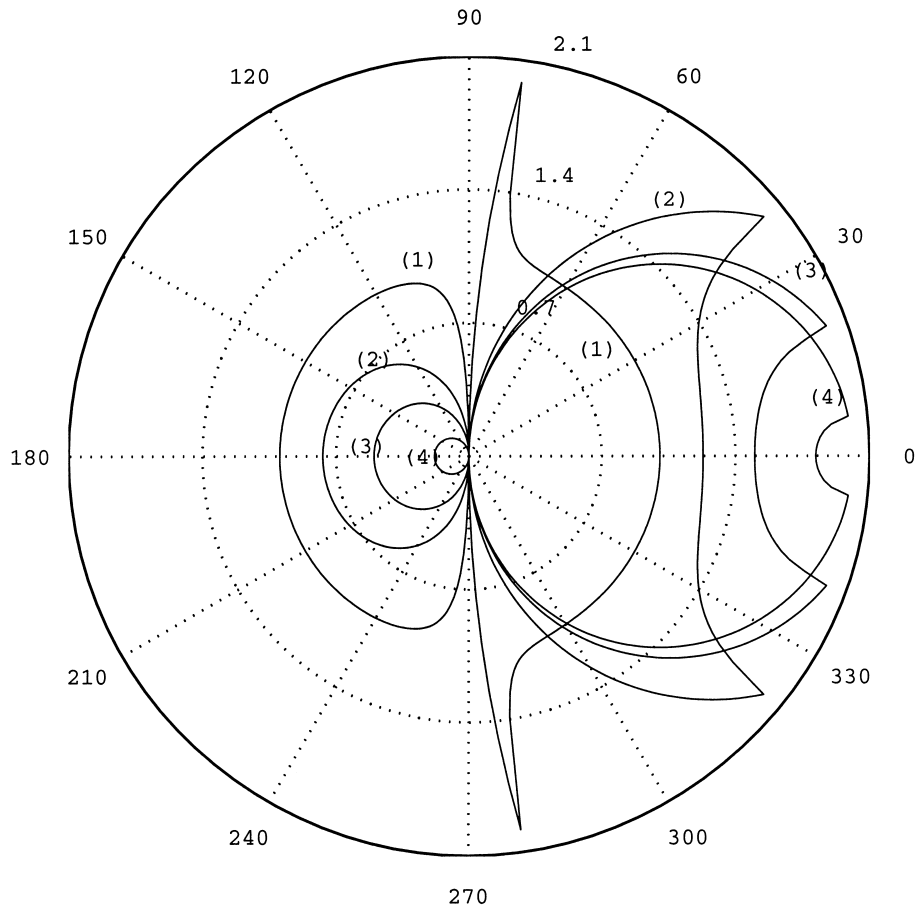


Fig. 4. Polar plot of the modulus of the far-field pattern $F(\theta; k)$ in the k_1 - k_3 case, for (1) $\tilde{k}_1 = k_3/k_1 = 1.01$, (2) $\tilde{k}_1 = 1.6$, (3) $\tilde{k}_1 = 3$ and (4) $\tilde{k}_1 = 10$, corresponding to critical angles (1) $\theta_c=81.9^\circ$, (2) $\theta_c=38.6^\circ$, (3) $\theta_c=19.4^\circ$ and (4) $\theta_c=5.7^\circ$, respectively.

where

$$F(\theta; k) = \frac{2|\cos \theta|}{|\cos \theta| + \sqrt{\tilde{k}_m^2 - \sin^2 \theta}}, \quad m = 1, 3, \tag{3.10b}$$

is the source far-field pattern.¹ The parameters \tilde{k}_m , $m=1,3$ appearing in the above equation are defined as follows:

$$\tilde{k}_1 = \frac{k_3}{k_1} > 1, \quad \tilde{k}_3 = \frac{k_1}{k_3} = \sin \theta_c < 1, \tag{3.10c}$$

where θ_c is the critical angle.

We can clearly observe in Eqs. (3.10a)–(3.10c) the geometrical spreading law, and that the far-field wave pattern exhibits a strong azimuthal anisotropy. The main features of this anisotropy are the formation of a shadow zone centered along the parameter (wavenumber) irregularity ($\theta=90^\circ$) and that, as $x \rightarrow \pm\infty$ in the two sectors not including the parameter irregularity, the asymptotic behavior of the far-field approaches the standard one, corresponding to

¹ The error term predicted by the stationary phase method in Eq. (3.10a) is actually $O(k_*R)^{-1}$, but in the present case it is known that the next contribution to the far-field comes from the branch-cut integrals and is of order $O(k_*R)^{-3/2}$.

cylindrical outgoing waves, propagating in $D^{(m)}$, $m=1, 3$, with the wavelengths at infinity $\lambda_m=2\pi/k_m$, respectively. All the above features are also demonstrated in Fig. 4, which is a polar plot of the modulus of the far-field pattern $F(\theta; k)$ for various characteristic values of $\tilde{k}_1 = 1.01, 1.6, 2$ and 10 , corresponding to critical angles $\theta_c=81.9^\circ, 38.6^\circ, 19.4^\circ$ and 5.7° , respectively. We can observe in this figure the following facts concerning the far-field structure of the source-generated field in the k_1 - k_3 case:

1. As $\tilde{k}_1 \rightarrow 1$, $|F(\theta; k)| \rightarrow 1$, and the above results tend to the far-field asymptotics of the source in a uniform medium.
2. As \tilde{k}_1 increases, the width of the shadow (centered at $\theta=90^\circ$) also increases, and for $\tilde{k}_1 \rightarrow \infty$ the shadow tends to expand to the whole subdomain $D^{(1)}$. At the same time the complementary region (the subdomain $D^{(3)}$ corresponding to the greater wavenumber) becomes the propagating wave zone.
3. For intermediate values of \tilde{k}_1 , the azimuthal anisotropy of the far-field is stronger in $D^{(3)}$. This is because, except the variation from the shadow (centered at $\theta=90^\circ$) to the wave zone (centered at $\theta=0^\circ$ and 180° , respectively), in $D^{(3)}$ the radical of the denominator of Eq. (3.10b) changes sign (see Eq. (3.10c)) at the value $\theta=\theta_c$ producing the peaks appearing at the critical angle.

In order to illustrate the closeness between the leading asymptotic approximation and the complete solution, comparisons between the analytical solution, given by Eqs. (3.3) and (3.4), and the far-field asymptotic approximation, Eqs. (3.10a)–(3.10c), are presented in Figs. 5 and 6, in the case of a discontinuous medium with $k_1=0.2798 \text{ m}^{-1}$ and $k_3=0.4463 \text{ m}^{-1}$. In this case the ratio $\tilde{k}_1 = 1.6$. These wavenumbers correspond to water waves emitted from a pulsating source at a frequency $\omega=1.6 \text{ rad s}^{-1}$ and propagating at depths $h_1=6 \text{ m}$ and $h_3=1.5 \text{ m}$, with wavelengths $\lambda_1=22.45 \text{ m}$ and $\lambda_3=14.08 \text{ m}$, respectively (see also Section 4.3). The real part of the wave potential in the near field is presented in Fig. 5 by using equipotential lines. We can observe the similarity between the two patterns outside of a few wavelengths range from the source.

In Fig. 6 a comparative polar plot of the modulus and the phase of the source-generated field at an intermediate range ($R=150 \text{ m}$) from the source is presented. The small discrepancies between the analytical solution and its far-field asymptotic approximation in the sector $\theta \in [\theta_c=38.6^\circ, 90^\circ]$ and its symmetric with respect to the x -axis are due to the effect of the lateral wave, which is more profound there. As already mentioned, this is a lower order $O(k_*R)^{-3/2}$ diffraction component, that can also be predicted in the far-field by including the branch-cut integral contributions. See also Refs. [1,24].

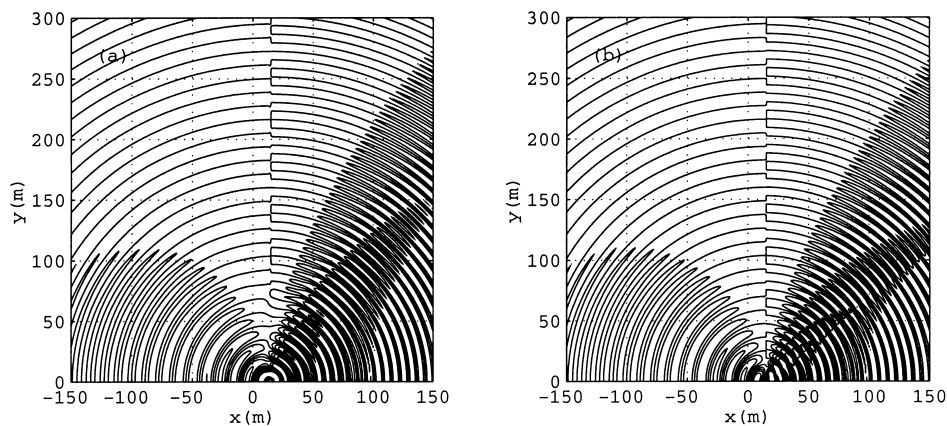


Fig. 5. Real part of the source field in the k_1 - k_3 case, for $k_1=0.2798 \text{ m}^{-1}$ and $k_3=0.4463 \text{ m}^{-1}$, corresponding to water waves of frequency $\omega=1.6 \text{ rad s}^{-1}$ at depths $h_1=6 \text{ m}$ and $h_3=1.5 \text{ m}$, respectively. Comparison between (a) the analytical solution Eq. (3.4) and (b) the principal far-field asymptotic approximation, Eqs. (3.10a)–(3.10c).

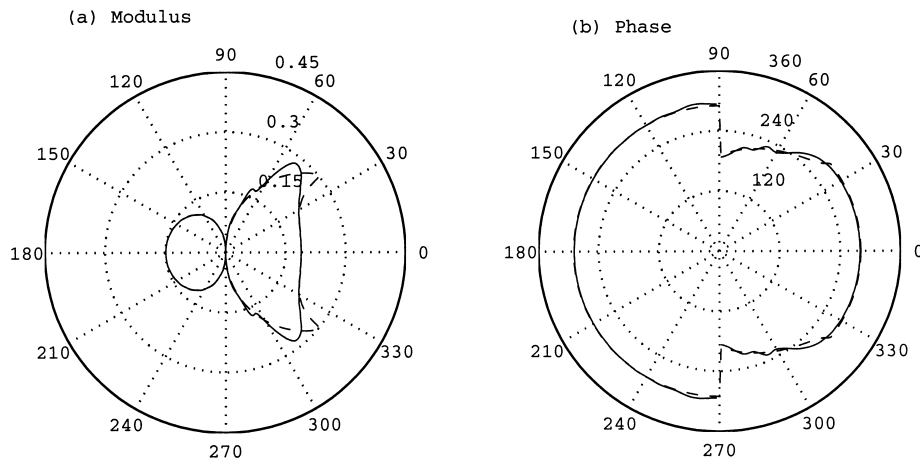


Fig. 6. Polar plots of (a) the modulus and (b) the phase of the source field in the k_1 - k_3 case, with $k_1=0.2798 \text{ m}^{-1}$ and $k_3=0.4463 \text{ m}^{-1}$, at an intermediate range $R=150 \text{ m}$ a few wavelengths from the source. Comparison between the analytical solution (solid lines) and the principal far-field asymptotic approximation (dashed lines).

4. Numerical Fourier inversion of the transformed wave potential

The numerical solution of the boundary value problem $\mathcal{P}_\xi^T(k, x_0)$, Eqs. (2.9a) and (2.9b), in conjunction with the representations (2.8) in the two semi-infinite intervals $d^{(m)}$, $m=1,3$, enables us to calculate the transformed wave potential $\varphi(x, x_0; \xi)$ for any wavenumber distribution $k(x)$ of the form (2.1) and throughout the whole real axis $x \in \mathbb{R}$. The last, but not trivial, step required in order to obtain the solution of the problem in the physical domain is to carry out the Fourier inversion, by using either the standard formula (2.4b) or its complex counterpart, Eq. (2.14). The complex Fourier inversion will be applied in the present work, permitting us an efficient and robust calculation of the source field by means of the *fast Fourier transform* (FFT), and eliminating the aliasing problem due to the (numerical) undersampling of the integrand.

4.1. The path of integration in the complex ξ -plane

Assuming that, for all $x \in \mathbb{R}$, the transformed wave potential $\varphi(x, x_0; \xi)$ is well-behaved at infinity as $\xi \rightarrow \infty$ in S_{c0}^+ , the contour of integration associated with the inverse Fourier transform (2.14) can be arbitrarily deformed into a new path (C^+), as shown in Fig. 7. This path is composed of the following three parts: $(C_1^+) = \{\xi_1 = 0, -\tau < \xi_2 < 0\}$, $(C_2^+) = \{0 < \xi_1 < \mathcal{E}, \xi_2 = -\tau\}$, and $(C_3^+) = \{\mathcal{E} < \xi_1 < \infty, \xi_2 = -\tau\}$, where $\tau > 0$ is a small

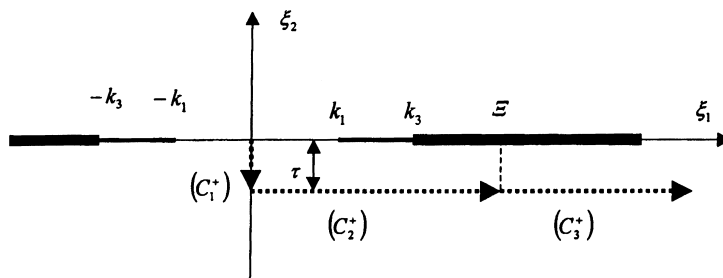


Fig. 7. The path of integration for the numerical Fourier inversion. The branch cuts associated with $\xi = \pm k_1, \pm k_3$ are denoted by thick lines.

positive number. Thus, the Fourier integral (2.14) can be equivalently put in the form

$$\begin{aligned}\Phi(\mathbf{r}, \mathbf{r}_0; \mu) &= 2 \int_{(C_1) \cup (C_2) \cup (C_3)} \varphi(x, x_0; \xi) \cos(\xi y) d\xi \\ &= 2 \int_{\xi_2=-\tau}^{\xi_2=\tau} \varphi(x, x_0; i\xi_2) \cosh(\xi_2 y) d\xi_2 + \exp(\tau y) \int_{\xi_1=-\mathcal{E}}^{\mathcal{E}} \varphi(x, x_0; |\xi_1| - i\tau) \exp(i\xi_1 y) d\xi_1 \\ &\quad - 2 \sinh(\tau y) \int_{\xi_1=0}^{\mathcal{E}} \varphi(x, x_0; \xi_1 - i\tau) \exp(-i\xi_1 y) d\xi_1 + 2 \int_{\xi_1=\mathcal{E}}^{\infty} \varphi(x, x_0; \xi) \cos((\xi_1 - i\tau)y) d\xi_1.\end{aligned}\quad (4.1)$$

The first term in the right-hand side of Eq. (4.1) is the integral along (C_1^+) , the second and the third terms together are equivalent to the integral along (C_2^+) and the fourth term is the integral along (C_3^+) . If τ is an appreciably small number, then, for moderate transverse ranges (y), the first and the third integrals in the right-hand side of Eq. (4.1) can be disregarded without significant loss in accuracy.

If $\mathcal{E} > 0$ is selected to be appropriately large ($\mathcal{E} \gg k_*$), the contribution of the fourth integral in the right-hand side of Eq. (4.1) can be efficiently approximated by using the large- ξ asymptotics of the wave potential (2.7b) as follows:

$$2 \int_{\xi_1=\mathcal{E}}^{\infty} \varphi(x, x_0; \xi) \cos((\xi_1 - i\tau)y) d\xi_1 \approx \int_{\xi=\mathcal{E}}^{\infty} \frac{\exp(-\xi_1|x - x_0|)}{\xi_1} d\xi_1 = \operatorname{Re}\{E_1(\mathcal{E}(|x - x_0| + iy))\}, \quad (4.2)$$

where the last integral has been analytically calculated, see ([29], paragraph 3.944 (4)) in terms of the exponential integral E_1 , as defined by Abramowitz and Stegun [30]. Thus, we have arrived at the following result:

$$\Phi(\mathbf{r}, \mathbf{r}_0; k) \approx \exp(\tau y) \int_{\xi_1=-\mathcal{E}}^{\mathcal{E}} \varphi(x, x_0; |\xi_1| - i\tau) \exp(i\xi_1 y) d\xi_1 + \operatorname{Re}\{E_1(\mathcal{E}(|x - x_0| + iy))\}. \quad (4.3)$$

It should be noted here that the second part in the right-hand side of Eq. (4.3), which includes the exponential integral, offer us a good representation of the numerical solution even in the neighborhood of the singularity ($x=x_0, y=0$).

On the basis of the above considerations, and under the assumption that for small $c > \tau > 0$, $\varphi(x, x_0; \xi)$ remains regular in the strip $\xi \in S_{c0}^+$ and well-behaved at infinity, Eq. (4.3), in conjunction with an application of FFT, can be used for obtaining the numerical solution of the problem in the general $k(x)$ case.

4.2. Numerical inversion by application of the fast Fourier transform

Noting that, for all $x \in \mathbb{R}$, the Fourier integral in the right-hand side of Eq. (4.3) is required (and thus, has to be calculated) for many discrete ranges (y), this term can be very efficiently calculated by means of FFT; see, e.g., [31]. Consider the following discretization of the interval $\xi \in [0, \mathcal{E}]$ into a finite number (N) of equal-length segments, with endpoints

$$\xi_l = (l - 1)\Delta\xi, \quad l = 1, \dots, N + 1, \quad \text{where } \Delta\xi = \frac{\mathcal{E}}{N}. \quad (4.4)$$

Let also the interval $y \in [0, Y]$ in the physical space be subdivided into the same number equal-length segments Δy , as follows:

$$y_j = (j - 1)\Delta y, \quad j = 1, \dots, N + 1, \quad \text{where } \Delta y = \frac{\pi}{\Delta\xi N} \quad \text{and } Y = N\Delta y = \frac{\pi}{\Delta\xi}. \quad (4.5)$$

Moreover, consider the following even extension of the array $\{\varphi_l = \varphi(\xi_l - i\tau), l=1, \dots, N+1\}$, $\tau > 0$ to $l=N+2, \dots, 2N$:

$$\varphi_l = \varphi_l, \quad l = 1, \dots, N + 1, \quad \varphi_{2N-l+2} = \varphi_l, \quad l = 2, 3, \dots, N. \quad (4.6)$$

Thus, the total length of the extended array is an even number: $M=2N$. On the basis of the above considerations, the integration in the right-hand side of Eq. (4.3) over the finite interval $\xi \in [-\mathcal{E}, \mathcal{E}]$ is written in the following discrete form:

$$\frac{\Phi(y_j)}{\exp(\tau y_j)} = \Delta\xi \left\{ \sum_{l=1}^{2N} \varphi_l \exp \left[i \frac{2\pi(l-1)(j-1)}{2N} \right] \right\}, \quad j = 1, \dots, N+1. \tag{4.7}$$

The summation in Eq. (4.7) can be very efficiently performed, simultaneously for all ranges $y=y_j, j=1, \dots, N+1$ by applying FFT to the array $\{\varphi_l, l=1, M\}$, if N is selected to be a power of 2. The problem with the application of FFT (and of DFT, in general) is that undersampling in the Fourier ξ -domain causes aliasing in the physical y -domain, due to the periodicity assumed by the discrete Fourier transform. Actually, the evaluation of the right-hand side of Eq. (4.7) does not yield the values of the function $\Phi(x, y_j, \mathbf{r}_0; k)/\exp(\tau y_j)$, at the points $y=y_j, j=1, \dots, N+1$, but rather $\sum_{n=-\infty}^{\infty} \Phi(x, y_j + 2nY, \mathbf{r}_0; k)/\exp(\tau(y_j + 2nY))$; see, e.g., Refs. [31,32]. Taking this fact into account, we obtain from Eq. (4.7) the following result:

$$\begin{aligned} \Phi(x, y_j, \mathbf{r}_0; k) &= \Delta\xi \exp(\tau y_j) \sum_{l=1}^{2N} \varphi_l \exp \left[i \frac{2\pi(l-1)(j-1)}{2N} \right] \\ &\quad - \sum_{n \neq 0} \Phi(x, y_j + 2nY, \mathbf{r}_0; k) \exp(-2\tau nY), \quad j = 1, \dots, N+1. \end{aligned} \tag{4.8}$$

The aliasing effect from (physical) ranges $|y|>Y$ is included in the second sum of the right-hand side of Eq. (4.8). It is clear from the same equation that by moving the integration contour in the complex domain, i.e. for $\tau>0$, the aliasing effect will be attenuated by at least a factor $\exp(-2\tau Y)$. On the other hand, τ cannot be too large because Eq. (4.3) is derived on the basis that the first and third integrals of Eq. (4.1) can be approximately dropped, which is possible only for appreciably small values of τ . Thus, there is a relation between the expected accuracy by the numerical Fourier inversion and the selection of the parameters τ, \mathcal{E} and N .

Extensive numerical evidence has shown that a value of $\mathcal{E} \approx 4-6k_*$ is large enough in order to use the asymptotics (2.7b) and obtain the contribution from the integral along the contour (C_3^+) analytically. In all examples that will be presented later on in the this paper, we have used a sampling of the interval $[-\mathcal{E}, \mathcal{E}]$ consisting of $M=2^{10}=1024$ points, and a shifting of the integration contour in $S_{c_0}^+$ by $\tau \approx \Delta\xi$. This choice results in an elimination of the aliasing effect by a factor at least 0.002, and has been proved small enough for disregarding the contributions of the first and third integrals in the right-hand side of Eq. (4.1) to the numerical solution.

In concluding this subsection, it should be mentioned that for the solution of the transmission problem (2.9a) and (2.9b) a finite difference scheme is used. For any value of the Fourier parameter ξ , the discrete system is constructed by using central, second-order finite differences to approximate the derivatives in Eq. (2.9a). Discrete boundary conditions are obtained by combining Eqs. (2.9a) and (2.9b) and then using central differences to approximate derivatives. Thus, the discrete scheme obtained in this way is uniformly of second order in the x -direction. Moreover, a number of about 20 points per horizontal wavelength is found to be sufficient to obtain accurate results.

4.3. Numerical examples

As a first demonstration of the numerical Fourier inversion scheme, we shall present calculated results in the k_1-k_3 case for which an analytical result is available, Eqs. (3.3) and (3.4). Comparisons between the solution obtained by the numerical Fourier inversion, Eq. (4.8), and the analytical solution, Eqs. (3.3) and (3.4), for the discontinuous medium with wavenumbers $k_1=0.2798 \text{ m}^{-1}$ (corresponding to a wavelength $\lambda_1=22.45 \text{ m}$) and ($k_3=0.4463 \text{ m}^{-1}$) ($\lambda_3=14.08 \text{ m}$), and for various values of the azimuthal angle θ are presented in Figs. 8 and 9. More specifically, Fig. 8 presents numerical vs. analytical solution for $\theta=90^\circ$, i.e. along the parameter irregularity, and for the first 100 m range from the source. The corresponding plots for $\theta=0^\circ$ and 45° in $d^{(3)}$, and for $\theta=135^\circ$ and 180° in $d^{(1)}$, are

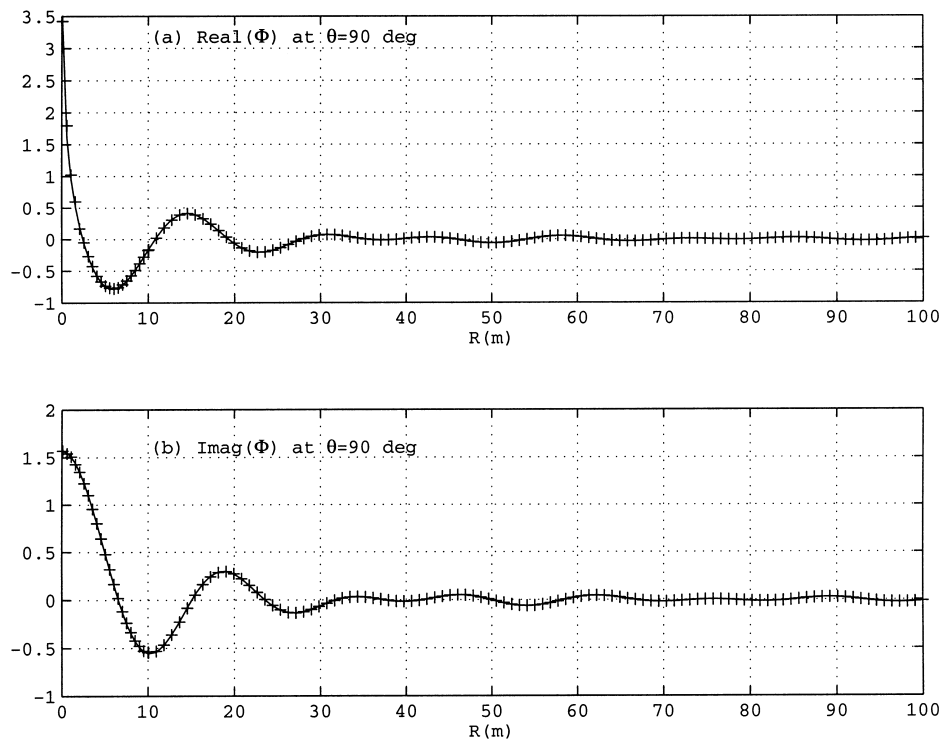


Fig. 8. Comparison between the analytical solution (solid line) and the numerical Fourier inversion (indicated by crosses) in the k_1 - k_3 case, with $k_1=0.2798 \text{ m}^{-1}$ and $k_3=0.4463 \text{ m}^{-1}$, at $\theta=0^\circ$ and in the first 100 m range from the source: (a) real part of the wave potential; (b) imaginary part of the wave potential.

presented in Fig. 9. In both figures the analytical solution results are plotted by using solid lines and the numerical results by using crosses. We can observe the remarkable accuracy of the numerical Fourier inversion scheme, even in the vicinity of the singular point.

As a next example, a monotonic bottom profile, of the form of a smooth underwater step, is considered. In this case the depth function is selected to be

$$h(x) = \begin{cases} h_1 = 6 \text{ m}, & x < a = 0, \\ \frac{h_1 + h_3}{2} - \frac{h_1 - h_3}{2} \tanh\left(3\pi\left(\frac{x}{b} - \frac{1}{2}\right)\right), & a < x < b, \\ h_3 = 1.5 \text{ m}, & x > b = 30 \text{ m}. \end{cases} \quad (4.9)$$

The bottom along with the corresponding wavenumber profile $k(x)$, obtained by means of Eq. (1.3) for a source frequency $\omega=1.6 \text{ rad s}^{-1}$, is plotted in Fig. 10. As previously, the wavelength ranges from $\lambda_1=22.45 \text{ m}$, for $x < a=0 \text{ m}$, to $\lambda_3=14.08 \text{ m}$, for $x > b=30 \text{ m}$, implying that both ratios $h_1/\lambda_1=0.26$ and $h_3/\lambda_3=0.1$ fall outside the limits of the deep or the shallow water theory. A second non-monotonic bed profile, which is produced by superposing a small bump to the former profile, will also be considered for computations. The latter, non-monotonic profile together with the corresponding wavenumber distribution are also plotted in Fig. 10.

In the case of the monotonic bottom profile the calculated wave field generated by a source located at $x_0=15 \text{ m}$, in the middle of the variable-depth interval, is presented in Fig. 11(a) by using equipotential lines. The wave pattern presents a noticeable similarity with the corresponding k_1 - k_3 case, shown in Fig. 5. Once again we observe the formation of the shadow zone along the parameter irregularity, with an ever expanding width as the range

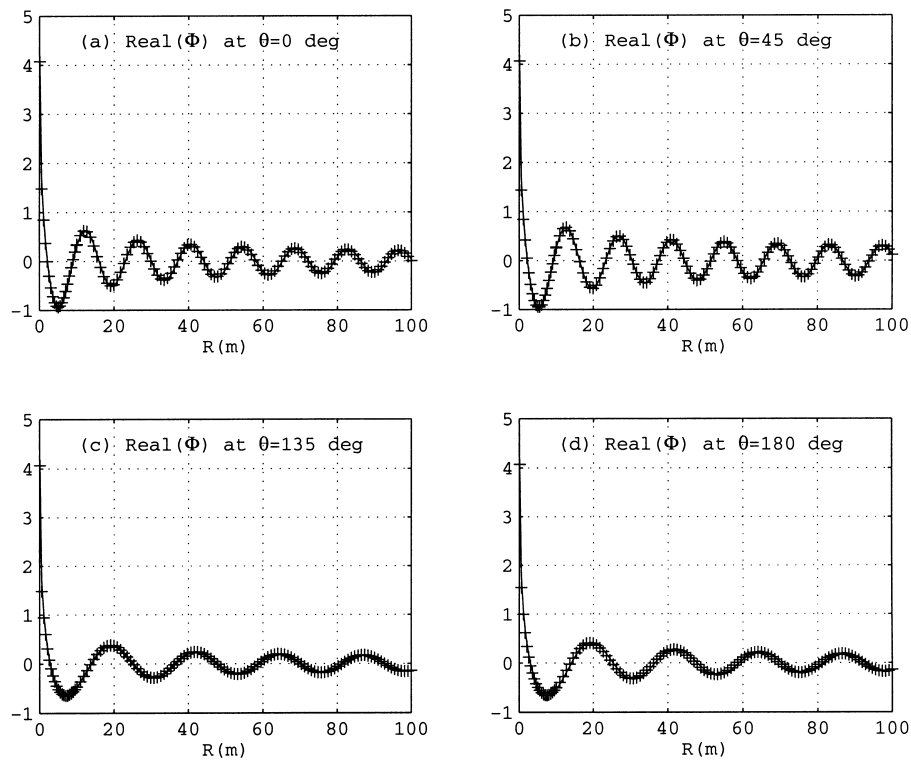


Fig. 9. Comparison between the analytical solution (solid line) and the numerical Fourier inversion (indicated by crosses) in the k_1 - k_3 case, with $k_1=0.2798 \text{ m}^{-1}$ and $k_3=0.4463 \text{ m}^{-1}$, in the first 100 m range from the source. Real part of the wave potential: (a) at $\theta=0^\circ$; (b) at $\theta=45^\circ$; (c) at $\theta=135^\circ$; (d) at $\theta=180^\circ$.

$R = \sqrt{|x - x_0|^2 + y^2}$ increases, and that the wave field behaves like outgoing cylindrical waves in the two sectors not including the parameter irregularity, propagating with wavelengths λ_1 and λ_3 , respectively. Extensive numerical evidence has shown that the above behavior is characteristic for the class of monotonic bottom/wavenumber profiles, justifying thus the study of the k_1 - k_3 case as a prototype. We can also note in Fig. 11(a) the appearance of the lateral waves in the azimuthal interval $[\theta_c, 90^\circ]$, which is more distinguishable in the present than in the corresponding k_1 - k_3 case; compare Figs. 11(a) and 5(a).

The above situation can be completely changed in the case of a non-monotonic bottom profile of the form of a smooth underwater ridge, as the second profile plotted in Fig. 10. If the position of the source is taken to be at (or near) the top of the ridge, a duct can be formed along the bottom irregularity (at $\theta=90^\circ$), as it is clearly illustrated in Fig. 11(b). In this case, the wave energy penetrating in the duct is trapped, and the strength of the wave field does not attenuate with range inside the duct. The above result clearly demonstrates the significance of the study of the Green's function of the mild-slope equation in connection with the rigor of the formulation of the diffraction problem of water waves by a 2D inhomogeneity in a shoaling environment, and especially as regards the quantification of the radiation condition (1.7).

5. Far-field structure of the source field in the case of a monotonic bed profile

The numerical Fourier inversion scheme described in the previous section is accurate at small or intermediate ranges from the source. This is true since, for large y , the contributions of the first and the third integrals in the

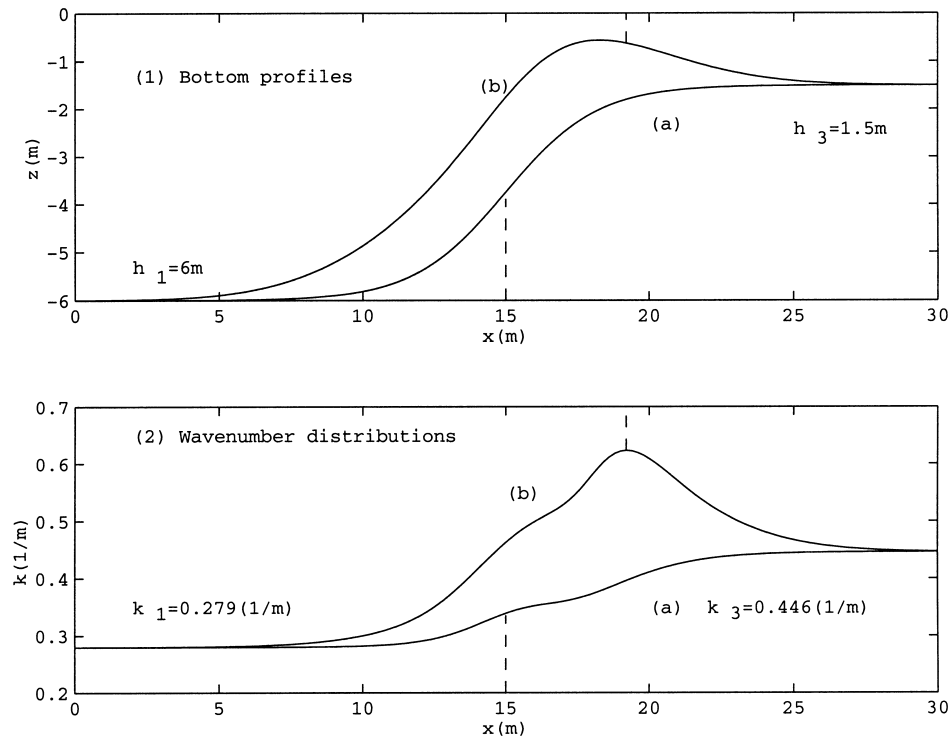


Fig. 10. (1) Bottom profiles and (2) wavenumber profiles, for water waves emitted from a source at a frequency $\omega = 1.6 \text{ rad s}^{-1}$, considered for computations: (a) monotonic bottom/wavenumber profiles; (b) non-monotonic bottom/wavenumber (of the form of a smooth underwater ridge). In both cases the position of the source (x_0) is indicated by using dashed lines.

right-hand side of Eq. (4.1) may become significant. Thus, in the present section we shall derive the far-field asymptotic approximation of the Fourier integral (2.14) in the case of a monotonic bed and wavenumber profiles of the form (2.1).

To start with, we shall introduce some additional notation. Let $\varphi(x, x_0; \xi)$, given by Eqs. (3.2a) and (3.2b), and $g(x, x_0; \xi)$ denote the solutions of the transformed problem $\mathcal{P}_\xi(k, x_0)$ in the k_1 - k_3 case, and in the general $k(x)$ case,

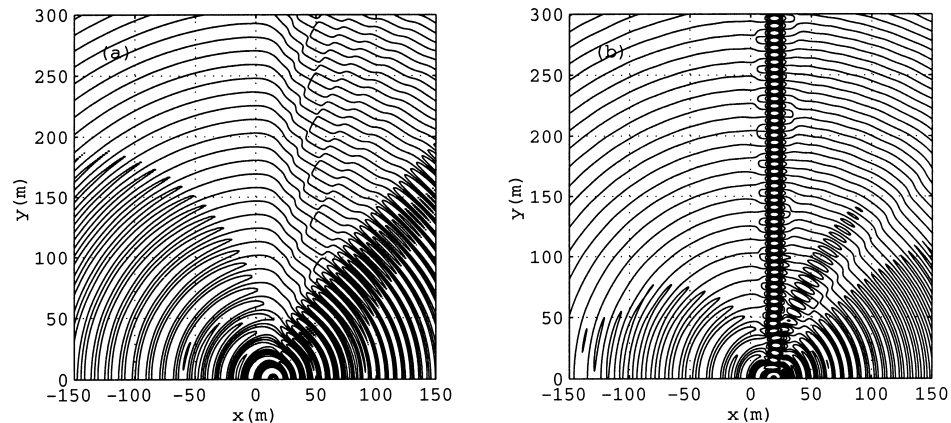


Fig. 11. Real part of the calculated wave field for the two bottom/wavenumber profiles shown in Fig. 10.

respectively. The difference of the above distributions is defined as

$$\gamma(x, x_0; \xi) = g(x, x_0; \xi) - \varphi(x, x_0; \xi). \tag{5.1}$$

Let also $\Phi(\mathbf{r}, \mathbf{r}_0; k)$, $G(\mathbf{r}, \mathbf{r}_0; k)$ and $\Gamma(\mathbf{r}, \mathbf{r}_0; k)$ denote their Fourier counterparts. Obviously, both $\varphi(x, x_0; \xi)$ and $g(x, x_0; \xi)$ are continuous and bounded functions for all $x, x_0 \in \mathbb{R}$, exhibiting the same discontinuity in their first derivative at the position of the source $x=x_0$. Thus, their difference $\gamma(x, x_0; \xi)$ is a bounded and continuously differentiable function over the whole real axis, satisfying

$$\frac{\partial^2 \gamma(x, x_0; \xi)}{\partial x^2} + (k^2(x) - \xi^2)\gamma(x, x_0; \xi) = \delta k^2(x; x_0)\gamma(x, x_0; \xi), \quad -\infty < x < \infty, \tag{5.2a}$$

where

$$\delta k^2(x, x_0) = (k_1^2 + (k_3^2 - k_1^2)U(x - x_0)) - k^2(x), \tag{5.2b}$$

denotes the difference of the wavenumber distributions in the two cases. Since the point source is assumed to be located inside the variable parameter subinterval ($x_0 \in d^{(2)}$), the support of the above distribution is

$$\text{supp}\{\delta k^2(x; x_0)\} \subset d^{(2)}. \tag{5.3}$$

All three solutions $\varphi(x, x_0; \xi)$, $g(x, x_0; \xi)$ and $\gamma(x, x_0; \xi)$ are represented in the two semi-infinite intervals $d^{(1)} = (-\infty, a]$ and $d^{(3)} = [b, \infty)$ by means of Eq. (2.8). In the sequel we shall use the notation $C_\varphi^{(m)}(\xi)$, $C_g^{(m)}(\xi)$, $C_\gamma^{(m)}(\xi)$, $m = 1, 3$, in order to distinguish between the coefficients of their representations there. Note that by Eq. (3.2b) it holds

$$C_\varphi^{(1)}(\xi) = C_\varphi^{(3)}(\xi) = C_\varphi(\xi) = i/\tau(\xi), \quad \text{where } \tau(\xi) = \sqrt{k_1^2 - \xi^2} + \sqrt{k_3^2 - \xi^2}. \tag{5.4}$$

Now, by applying Green's theorem to Eqs. (5.2a) and (5.2b) we obtain

$$\gamma(x, x_0; \xi) = g(x, x_0; \xi) - \varphi(x, x_0; \xi) = - \int_{t=-\infty}^{\infty} \delta k^2(t; x_0)\varphi(t, x_0; \xi)g(x, t; \xi) dt \tag{5.5}$$

and by using Eq. (5.3) we arrive at the following integral equation:

$$g(x, x_0; \xi) + \int_{t=a}^{t=b} \delta k^2(t; x_0)\varphi(t, x_0; \xi)g(x, t; \xi) dt = \varphi(x, x_0; \xi). \tag{5.6}$$

The kernel of the above equation $\delta k^2(t; x_0)\varphi(t, x_0; \xi)$ is bounded and continuous everywhere except $t=x_0$, and thus, Fredholm theory is applicable, providing us existence of the solution of Eq. (5.6) for the given, continuous $\varphi(x, x_0; \xi)$. Moreover, by using the large ξ — asymptotics of the function $\varphi(x, x_0; \xi)$, which are easily derived from Eqs. (3.2a) and (3.2b), in conjunction with the ones of $g(x, x_0; \xi)$, given by Eq. (2.7), we obtain that the difference $\gamma(x, x_0; \xi)$ behaves like

$$|\gamma(t, x_0; \xi)| \sim \frac{1}{\xi^2}, \quad \text{as } \xi \rightarrow \infty. \tag{5.7}$$

The above estimate can be exploited to ensure existence of the solution of the integral equation (5.6), first for large and real ξ , and then in the entire complex domain as a meromorphic function; see, e.g., [33].

5.1. The structure and the ξ -singularities of the transformed potential

It is obvious from Eq. (5.6) that $g(x, x_0; \xi)$ has all the ξ -singularities of $\varphi(x, x_0; \xi)$. Moreover, by substituting the representations (2.8) of $\varphi(x, x_0; \xi)$, $g(x, x_0; \xi)$ and $\gamma(x, x_0; \xi)$ in the two semi-infinite intervals $d^{(1)} = (-\infty, a]$ and

$d^{(3)}=[b, \infty)$ in the integral equation (5.6), and using Eq. (5.4), we obtain after some algebra the following result concerning the coefficients of the representation of $g(x, x_0; \xi)$ in $d^{(m)}$, $m=1, 3$:

$$C_g^{(m)}(x_0; \xi) = \frac{C_\varphi(\xi)}{1 + C_\varphi(\xi)\Lambda^{(m)}(x_0; \xi)}, \quad m = 1, 3, \tag{5.8a}$$

where

$$\Lambda^{(m)}(x_0; \xi) = \int_{t=a}^b \delta k^2(t; x_0) E^{(m)}(t, x_0; \xi) \frac{C_g^{(m)}(t; \xi)}{C_g^{(m)}(x_0; \xi)} dt, \quad m = 1, 3, \tag{5.8b}$$

$$E^{(1)}(t, x_0; \xi) = \exp(iU(t, x_0)|x_0 - t|\tau(\xi)), \quad E^{(3)}(t, x_0; \xi) = \exp(iU(x_0, t)|x_0 - t|\tau(\xi)), \tag{5.8c}$$

and $C_\varphi(\xi)$ and $\tau(\xi)$ are defined by Eq. (5.4).

Let us assume that for any $\xi \in \mathbb{R}$ the denominator of the right-hand side of Eq. (5.8a) does not vanish. This is equivalent to the requirement that $C_\varphi(\xi)$, $\xi \in \mathbb{R}$, does not become an eigenvalue of the integral equation

$$C_g^{(m)}(x_0; \xi) + C_\varphi(\xi) \int_{t=a}^b [\delta k^2(t; x_0) E^{(m)}(t, x_0; \xi)] C_g^{(m)}(t; \xi) dt = 0, \quad m = 1, 3. \tag{5.9}$$

Extensive numerical evidence supports this conjecture for the class of the monotonic bottom/wavenumber profiles. Under the previous assumption we obtain from Eqs. (5.8a)–(5.8c) that the singularities of $g(x, x_0; \xi) = C_g^{(m)}(\xi; x_0)\exp(i|x - x_0|\tau(\xi))$, in $d^{(m)}$, $m=1, 3$, will be of the same kind as the ones of $\varphi(x, x_0; \xi)$; see Section 3.1. These branch-point singularities will be located at the same points ($\xi = \pm k_1, \pm k_3$) on the real ξ -axis, as in the k_1 - k_3 case. On the basis of the above observations we can now proceed to calculate the leading term of the source far-field asymptotics in the case of a general, monotonic bed/wavenumber profile by applying the stationary-phase method.

5.2. The far-field asymptotic structure of the solution for a monotonic profile

By substituting Eq. (2.8) into the Fourier inversion formula (2.4b), and restricting ourselves to the symmetrical part $y>0$ of the physical domain D , we obtain

$$G^{(m)}(\mathbf{r}, \mathbf{r}_0; k) = \int_{\xi=-\infty}^{\infty} C_g^{(m)}(\xi) \exp(ik_*RS^{(m)}(R, \theta; k)) d\xi, \quad m = 1, 3, \tag{5.10}$$

where the phase function $S^{(m)}(R, \theta; k)$ is the same as defined by Eq. (3.8). Note that the functions $C_g^{(m)}(\xi)$ do not involve the large parameter R , and thus, they do not contribute to the stationarity of the phase. Consequently, the points of stationarity of the phase function $S^{(m)}(R, \theta)$ are the same as in the k_1 - k_3 case, Eq. (3.9). Thus, we finally obtain

$$G^{(m)}(\mathbf{r}, \mathbf{r}_0; k) = \frac{i\pi}{2} \exp\left(i\left(k_m R - \frac{\pi}{4}\right)\right) \sqrt{\frac{2}{\pi k_m R}} F_m(\theta; k) + O\left(\frac{1}{k_* R}\right)^{3/2}, \quad m = 1, 3, \tag{5.11a}$$

where $F_m(\theta; k)$ is the far-field pattern in the monotonic $k(x)$ case, defined by

$$F_m(\theta; k) = -2ik_m C_g^{(m)}(x_0; k_m \sin \theta) |\cos \theta|, \quad m = 1, 3. \tag{5.11b}$$

It must be stressed here that Eqs. (5.11a) and (5.11b) are consistent, in the sense that, when $\delta k^2=0$, then $\Lambda_m=0$ and thus, the above formulae reduce to the corresponding ones obtained in the k_1 - k_3 case, Eqs. (3.10a)–(3.10c). Moreover, although the asymptotic estimates (5.11) are derived for the field point outside the region of parameter irregularity, $x \in D^{(m)}$, $m=1, 3$, at the same time and for large ranges ($R \rightarrow \infty$), i.e. actually in the far-field, they

become valid everywhere, except $\theta=90^\circ$ (and $\theta=270^\circ$). Consequently, the formation of the shadow zone is still predicted and in the general, monotonic $k(x)$ case. As in the k_1 - k_3 case, the next $O(k_*R)^{-3/2}$ term in the far-field asymptotics (5.11) is a diffraction component associated with the lateral wave, and can be predicted by including the branch-cut integral contributions. However, it is more important here to calculate this term for $\theta=90^\circ$, where, as indicated by Eqs. (5.11a) and (5.11b), the principal $O(k_*R)^{-1/2}$ term vanishes. In this case the Fourier integral is

$$G^{(m)}(x = x_0, y, \mathbf{r}_0; k) = \int_{\xi=-\infty}^{\infty} g(x = x_0, x_0; \xi) \exp(iy\xi) d\xi, \tag{5.12}$$

and the phase has no point of stationarity. The leading asymptotic term comes exclusively from the branch-point contributions, and is calculated to be ([1], Chapter 4.8; [2])

$$G^{(m)}(x = x_0, y, \mathbf{r}_0; k) = 2\sqrt{\pi} \exp(-i\pi/4) \{A_1\sqrt{k_1} \exp(ik_1y) - A_3\sqrt{k_3} \exp(ik_3y)\} y^{-3/2}, \tag{5.13}$$

where

$$A_m = - \lim_{\xi \rightarrow k_m} \sqrt{\frac{\xi - k_m}{k_m}} \frac{\partial g(x_0; \xi)}{\partial \xi}, \quad m = 1, 3. \tag{5.14}$$

We observe from Eq. (5.13) that the wave field along the bottom irregularity ($\theta=90^\circ, 270^\circ$) has an amplitude of order $O(R^{-3/2})$ and consists of the superposition of two outgoing waves with wavelengths corresponding to the two depths at infinity. Moreover, it can be easily verified that the above result is compatible with the analytical solution, Eq. (3.3), in the k_1 - k_3 case.

For the monotonic bed/wavenumber profile (4.9), shown also in Fig. 10, two images (produced by using equipotential lines) of the real part of the source potential, in the first few wavelengths range from the source, are presented in Fig. 12. The left image is based on the numerical Fourier inversion scheme and the right image on the far-field asymptotic approximation, Eqs. (5.11a) and (5.11b), respectively. Moreover, a comparative polar plot of the modulus and the phase of the source field at an intermediate range of a few wavelengths from the source ($R=100$ m) is presented in Fig. 13, as calculated by the present numerical Fourier inversion scheme (solid lines) and as predicted by the principal asymptotic approximation (dashed lines), respectively. Again, we can clearly observe in these figures that the effect of the lateral wave in the azimuthal interval $[\theta_c, 90^\circ]$ is more evident in the present than in the corresponding k_1 - k_3 case.

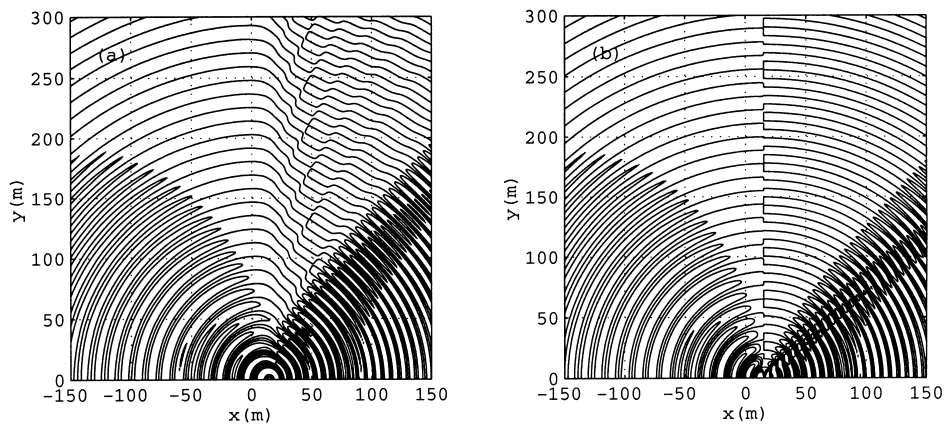


Fig. 12. Real part of the source field for the monotonic bottom/wavenumber profile shown in Fig. 10. Comparison between (a) the numerical Fourier inversion and (b) the principal far-field asymptotic approximation.

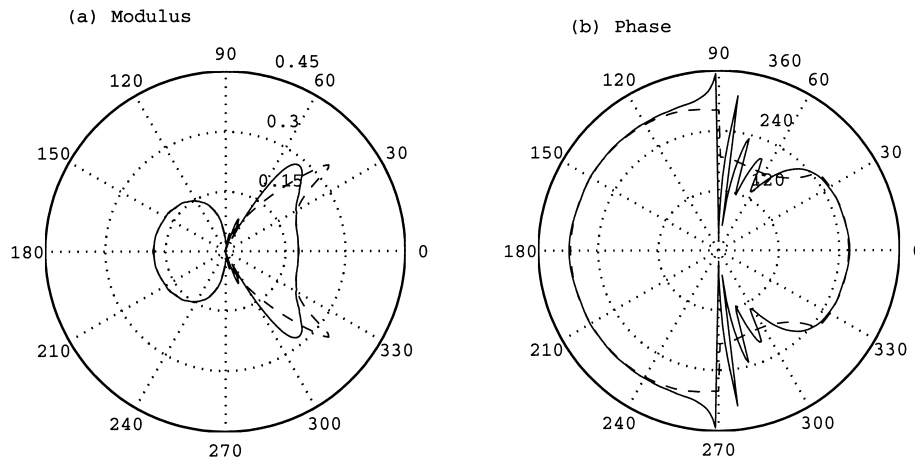


Fig. 13. Polar plots of (a) the modulus and (b) the phase of the source field for the monotonic bottom/wavenumber profile, shown in Fig. 10, at an intermediate range $R=150$ m from the source. Comparison between the numerical Fourier inversion (solid lines) and the principal far-field asymptotic approximation (dashed lines).

6. Conclusions

The present work has been concerned with the construction and study of the Green's function of the mild-slope equation, in a region characterized by an uneven bottom profile of arbitrary shape with different depths at infinity. In this sense, the present work is a prerequisite to the study of diffraction of water waves by localized bed irregularities over a 1D bottom shoaling, by means of the mild-slope equation and the Green's theorem. One of our main concerns in formulating and solving the source problem for the mild-slope equation is to investigate its far-field structure, which is expected to be strongly dependent on the azimuthal angle. For, the knowledge of the rate of decay of the wave amplitude and of the direction of propagation at large distances from the source (or the localized inhomogeneity) is a necessity for the quantification of the radiation condition and the formulation of the diffraction problem, and a valuable supplementary information for elaborating local ABC's, absorbing layers and/or infinite elements to better fit to any particular application. Moreover, an accurate numerical means for computing the Green's function is always attractive, not only for use where no other solution is available, but also as a check for existing asymptotic solutions, as the ones provided by the direct ray-optical (WKB) method and/or by the asymptotic evaluation of Fourier (or radiation) integrals [1,2].

The present analysis demonstrates that, in the case of a continuous, monotonic bed profile, the far-field pattern exhibits common features with the simply-discontinuous wavenumber case. The main characteristics of the far-field are: (i) the formation of a shadow zone with an ever expanding width, which is located along the bottom irregularity, where the wave amplitude is $O(R^{-3/2})$, and (ii) in each of the two sectors not including the parameter irregularity the asymptotic behavior of the wave field approaches the standard one, consisting of an outgoing wave propagating with an amplitude $O(R^{-1/2})$ and wavelength corresponding to the sector-depth at infinity. In the case of a non-monotonic bottom profile more complicated wave patterns can be produced, due to the phenomenon of wave trapping. It is demonstrated in the present work that wave trapping may arise along the bottom irregularity in the case of non-monotonic bed profiles, as, e.g., in the case of a smooth underwater ridge. Such an intricacy is associated with the emergence of additional pole-type singularities in the Fourier integrand. The calculation of trapping modes could be facilitated by the study of an eigenvalue integral equation, which is derived in the present work. A detailed analysis of this subject will be presented elsewhere.

Finally, it should be noticed that the present approach can be extended to treat the fully 3D problem of water waves emitted by a monochromatic point source in a variable-depth domain. First results in this direction have been presented in [34].

Acknowledgements

The author is grateful to Professor G.A. Athanassoulis (National Technical University of Athens) for his support and his valuable suggestions on the present work.

References

- [1] L.B. Felsen, N. Marcuvitz, *Radiation and Scattering of Waves*, Prentice-Hall, Englewood Cliffs, NJ, 1973.
- [2] L.M. Brekhovskikh, O.A. Godin, *Acoustics of Layered Media II. Point Sources and Bounded Beams*, Springer, Berlin, 1992.
- [3] C.C. Mei, *The Applied Dynamics of Ocean Surface Waves*, World Scientific, Singapore, 1989 (2nd reprint, 1994).
- [4] S. Massel, Extended refraction–diffraction equations for surface waves, *Coastal Eng.* 19 (1993) 97–126.
- [5] P.G. Chamberlain, D. Porter, The modified mild-slope equation, *J. Fluid Mech.* 291 (1995) 393–407.
- [6] J.W. Miles, P.G. Chamberlain, Topographical scattering of gravity waves, *J. Fluid Mech.* 361 (1998) 175–188.
- [7] N. Booij, A note on the accuracy of the mild-slope equation, *Coastal Eng.* 7 (1983) 191–203.
- [8] D. Porter, D.J. Staziker, Extensions of the mild-slope equation, *J. Fluid Mech.* 300 (1995) 367–382.
- [9] G.A. Athanassoulis, K.A. Belibassakis, A consistent coupled-mode theory for the propagation of small-amplitude water waves over variable bathymetry regions, *J. Fluid Mech.* 389 (1999) 275–301.
- [10] D. Givoli, Non-reflecting boundary conditions, *J. Comput. Phys.* 94 (1991) 1–29.
- [11] D. Givoli, *Numerical Methods for Problems in Infinite Domains*, Elsevier, Amsterdam, 1992.
- [12] S.V. Tsynkov, Numerical solution of problems in unbounded domains, *Appl. Numer. Math.* 27 (1998) 465–532.
- [13] J.C.W. Berkhoff, Linear wave propagation problems and the finite element method, in: R.H. Gallagher, J.T. Oden, C. Taylor, O.C. Zienkiewicz (Eds.), *Finite Elements in Fluids*, Vol. 1, Wiley, New York, 1975, pp. 251–264.
- [14] Y. Xu, Radiation condition and scattering problem for time-harmonic acoustic waves in a stratified medium with a nonstratified inhomogeneity, *IMA J. Appl. Math.* 54 (1995) 9–29.
- [15] R. Holford, Elementary source-type solution of the reduced wave equation, *J. Acoust. Soc. Am.* 70 (1981) 1427–1436.
- [16] Y.L. Li, C.H. Liu, S.J. Franke, Three-dimensional Green’s function for wave propagation in a linearly inhomogeneous medium — the exact analytic solution, *J. Acoust. Soc. Am.* 87 (1990) 2285–2291.
- [17] G.D. Manolis, R.P. Shaw, Green’s function for the vector wave equation in a mildly heterogeneous continuum, *Wave Motion* 24 (1996) 59–83.
- [18] R. Raspet, S.W. Lee, E. Kuester, D.C. Chang, W.F. Richards, R. Gilbert, N. Bong, A fast-field program for sound propagation in a layered atmosphere above an impedance ground, *J. Acoust. Soc. Am.* 77 (1985) 345–352.
- [19] T.L. Richards, K. Attenborough, Accurate FFT-based Hankel transforms for predictions of outdoor sound propagation, *J. Sound Vib.* 109 (1986) 157–167.
- [20] F.R. Di Napoli, R.L. Deavenport, Theoretical and numerical Green’s function solution in a plane layered medium, *J. Acoust. Soc. Am.* 67 (1980) 92–105.
- [21] F.B. Jensen, W.A. Kuperman, M.B. Porter, H. Schmidt, *Computational Ocean Acoustics*, AIP Press, New York, 1994.
- [22] A.G. Ramm, *Multidimensional Inverse Scattering Problems*, Longman, New York, 1992.
- [23] B. Noble, *Methods Based on the Wiener–Hopf Technique*, Chelsea, New York, 1988.
- [24] N. Bleistein, *Mathematical Methods for Wave Phenomena*, Academic Press, New York, 1984.
- [25] Y.A. Brychkov, A.P. Prudnikov, *Integral Transforms of Generalized Functions*, Gordon and Breach, London, 1989.
- [26] V.S. Vladimirov, *Generalized Functions in Mathematical Physics*, MIR, Moscow, 1979.
- [27] D.C. Champeney, *A Handbook of Fourier Theorems*, Cambridge University Press, Cambridge, 1987.
- [28] Y.V. Sidorov, M.V. Fedoryuk, M.I. Shabunin, *Lectures on the Theory of Complex Functions*, MIR, Moscow, 1985.
- [29] I.S. Gradshteyn, I.M. Ryzhik, *Tables of Integrals Series and Products*, Academic Press, New York, 1965.
- [30] M. Abramowitz, I.A. Stegun, *Handbook of Mathematical Functions*, Dover, New York, 1964.
- [31] A.V. Oppenheim, R.W. Schaffer, *Discrete-Time Signal-Processing*, Prentice-Hall, Englewood Cliffs, NJ, 1989.
- [32] N.C. Geckinkli, D. Yavuz, *Discrete Fourier Transformation and its Applications to Power Spectra Estimation*, Elsevier, Amsterdam, 1983.
- [33] E.A. Coddington, N. Levinson, *Theory of Ordinary Differential Equations*, McGraw-Hill, New York, 1955.
- [34] G.A. Athanassoulis, K.A. Belibassakis, Water-wave Green’s function for a 3D uneven-bottom problem with different depths at $x \rightarrow +\infty$ and $x \rightarrow -\infty$, in: *Proceedings of the IUTAM Symposium on Computational Methods for Unbounded Domains, Fluid Mechanics and its Applications*, Vol. 39, Kluwer Academic Publishers, Dordrecht, 1998, pp. 21–32.